X-ray diffraction of molybdenum under ramp compression to 1 TPa

Jue Wang,[1,*] Federica Coppari,[2] Raymond F. Smith,[2] Jon H. Eggert,[2] Amy E. Lazicki,[2] Dayne E. Fratanduono,[2] J. Ryan Rygg,[2] Thomas R. Boehly,[3] Gilbert W. Collins,[2] and Thomas S. Duffy[1]

[1]*Department of Geosciences, Princeton University, Princeton, New Jersey 08544, USA*

[2]*Lawrence Livermore National Laboratory, P.O. Box 808, Livermore, California 94550, USA*

[3]*Laboratory for Laser Energetics, University of Rochester, 250 East River Road, Rochester, New York 14623-1299, USA*

(Received 23 May 2016; revised manuscript received 25 June 2016; published 1 September 2016)

Molybdenum (Mo) is a transition metal with a wide range of technical applications. There has long been strong interest in its high-pressure behavior, and it is often used as standard for high-pressure experiments. Combining powder x-ray diffraction and dynamic ramp compression, structural and equation of state data were collected for solid Mo to 1 TPa (10 Mbar). Diffraction results are consistent with Mo remaining in the body-centered-cubic structure into the TPa regime. Stress-density data show that Mo under ramp loading is less compressible than the room-temperature isotherm but more compressible than the single-shock Hugoniot.

DOI: 10.1103/PhysRevB.94.104102

I. INTRODUCTION

Molybdenum (Mo) is a refractory 4*d* transition metal that adopts the body-centered-cubic (bcc) structure over a broad range of pressures and temperatures. It finds widespread technical applications due to its high melting point, high strength, and other attractive properties. Mo is an important material in high-pressure science. It has been studied extensively under shock compression [1–8] and has been used as a pressure calibrant in diamond anvil cell (DAC) experiments [9–12]. Static compression experiments have been used to explore its equation of state (EOS) and phase stability [13–15], melting behavior [16,17], thermoelastic properties [18–20], and shear strength [21]. Mo has been the subject of first-principles theoretical studies to explore various properties such as the crystal structure, melting, and elasticity at extreme conditions [22–27]. It also serves as a test case to understand the general behavior of transition elements at high levels of compression [23,28,29].

The crystal structure is the most fundamental property of a solid material and controls its physical and chemical behavior. The stable phase of Mo at several hundred GPa (several million atmospheres) pressures has been examined in a number of theoretical studies [22,24,30–39]. The bcc molybdenum is predicted to transform to either a face-centered-cubic (fcc) structure [24,31,32,37–39] or a double hexagonal-close-packed (dhcp) [35,36] structure between 600 and 700 GPa at 0 K (Fig. 1). Static DAC studies have shown that Mo remains in the bcc structure until at least 410 GPa at room temperature [11–13,15], although one early study claimed to reach as high as 560 GPa [14]. It remains very challenging to reach such multimegabar pressures with DAC technology [40]. Along the Hugoniot, Mo melts near 390 GPa [2,7,8], precluding the study of the solid phase to higher pressures by shock compression.

Ramp compression is a technique for dynamic loading of materials to very high pressures without the large temperature increases and sample melting associated with shock loading [41,42]. Ramp loading can be achieved in laser compression experiments by applying a time-dependent ramped increase in laser intensity onto a material surface. Ablation of the surface due to the absorbed laser energy leads to the propagation of a ramped loading wave into the sample. Recent developments in laser-based ramp compression allow pressures up to TPa (10 million atmosphere pressure) conditions to be reached for compression over nanosecond timescales [42–49]. The development of nanosecond (or faster) x-ray diffraction diagnostics provides a new means to probe the lattice compression and structural state of materials under these extreme conditions [49–54]. Previous laser compression experiments [7] used x-ray diffraction to explore the structure and melting of Mo under shock compression showing that Mo remains in the bcc structure until shock melting occurs near 390 GPa (Fig. 1). In this paper, we use laser-based ramp-wave loading with nanosecond x-ray diffraction to compress crystalline Mo to TPa pressures and to explore its structure and EOS under these extreme conditions.

II. EXPERIMENTAL TECHNIQUE

Experiments were performed at the Omega Laser Facility [55], a 351-nm, 60-beam laser that can deliver up to 500 J of energy per beam onto mm-sized targets. The target package consisted of a 4-μm-thick Mo foil or pellet glued between a 25-μm-thick single-crystal diamond ablator and a 60-μm-thick diamond window with $\sim$1 μm glue-layer thickness [Fig. 2(a)]. For experiments designed to reach greater than 0.6 TPa, the ablator included an additional layer of 10-μm-thick diamond coated with a 1-μm thickness of gold, which served to protect the sample from preheating prior to arrival of the compression pulse. The Mo samples were either a foil (99.9% purity, GoodFellow Corp.) or compressed powder (99.95% purity, 2–4 μm grain size, Alfa Aesar). The starting materials were characterized by x-ray diffraction. The foils showed a strong [011] fiber texture, while the Mo powder pellets showed no preferred orientation.

The sample package was mounted onto a 160-μm-diameter tantalum pinhole and placed on a $10\times10\,\mathrm{mm}^2$ aperture at the front of an x-ray diffraction enclosure with dimensions of

*Present address: School of Chemical Sciences and Fredrick Seitz Materials Research Laboratory, University of Illinois at Urbana-Champaign, Urbana, IL 61801, USA.

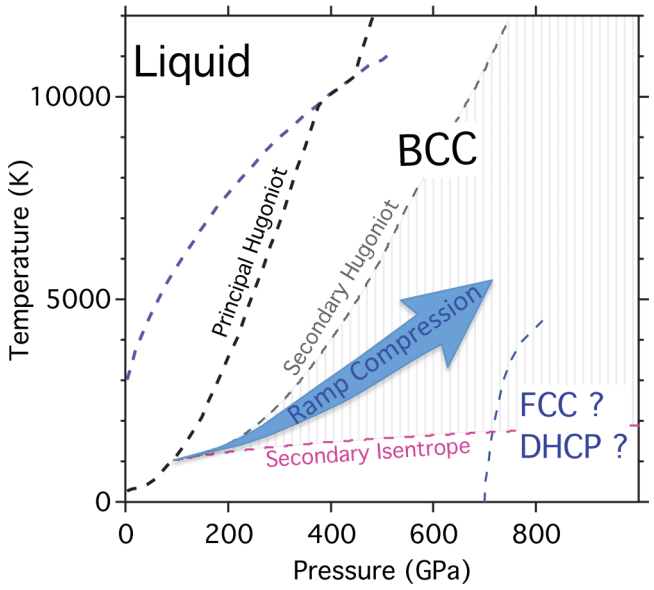

FIG. 1. Schematic phase diagram of molybdenum up to 1 TPa. The principal Hugoniot is shown as the dashed black curve [1,3]. The theoretically calculated melting curve [65] is shown as the dashed purple line. The dashed blue curve represents the theoretically predicted solid-solid phase boundary between the bcc and either fcc or dhcp phases at high pressure [33]. A schematic path for ramp compression is shown by the blue arrow and is bounded by the secondary Hugoniot (gray dashed curve) and secondary isentrope (magenta curve) for Mo (calculated using the SESAME EOS table 2984 [63]).

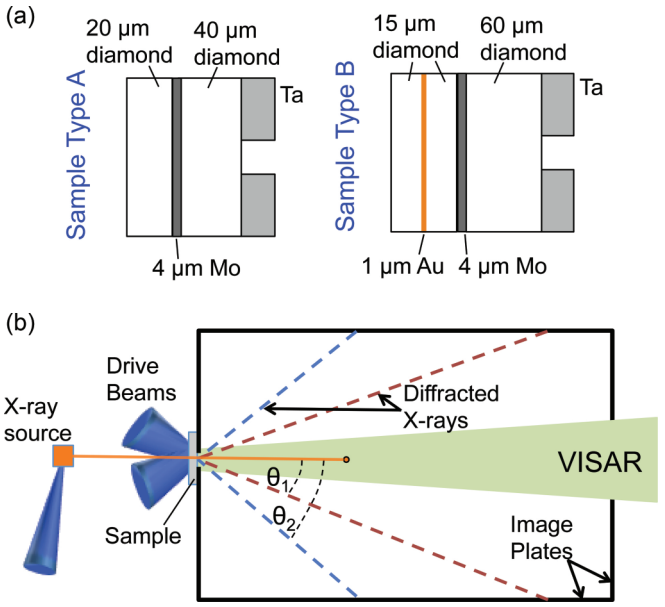

FIG. 2. (a) Schematic illustration of the target packages for ramp compression of Mo. Type A targets (pressure below 0.6 TPa) consist of a ∼4-μm-thick Mo foil or pellet held between a (110)-oriented single-crystal diamond ablator and window. For type B targets (pressure above 0.6 TPa), there is an additional layer of diamond and ∼1-μm thick Au layer serving as a shield to protect the sample from heating prior to the arrival of the compression wave. (b) Schematic illustration of angle-dispersive x-ray diffraction of ramp-compressed Mo (top view). The sample package is mounted on the front of a rectangular box. Beams from the Omega laser are used to both drive the sample to high pressures and generate a quasimonochromatic x-ray source. Diffracted x rays from the sample are recorded on image plates lining the box. The velocity of the rear surface of the target package is monitored using VISAR.

$50\times50\times75\,\mathrm{mm}^3$ [Fig. 2(b)]. A 25-mm diameter opening in the back of the diagnostic allows us to probe the velocity at the rear free surface of the diamond with a Velocity Interferometer System for Any Reflector (VISAR) [56]. The Omega laser was used to ablate the diamond front surface, producing an expanding plasma and driving a compression wave into the sample [45,49]. Either two or three time-separated Omega beams were applied to create a composite pulse shape in which the laser intensity was initially increased with a ramplike profile and then held for an additional period of time [Fig. 3(a)]. Specifically, one Omega laser beam with peak energy of 30–170 J in a 3.5-ns long ramp pulse was initially focused to an 800-μm diameter super-Gaussian spot onto the front surface of the diamond ablator. For experiments below 600 GPa, the initial ramp pulse was followed by applications of a 1-ns square pulse (130–360 J total energy). For higher pressure experiments, the initial pulse was instead followed by a pair of time-separated 1-ns square pulses (600–640 J total energy). These pulse configurations were designed to ramp compress and then hold the sample at a nearly constant peak pressure for several nanoseconds. Intensity variations in the input beams were smoothed by distributed phase plates. The required beam energies to achieve the desired pressure conditions with the Mo sample were estimated based on scaling relations from previous experiments that used a similar geometry for the target package [57].

As the compression wave propagates through the target, a series of reverberations generated at the Mo-diamond interfaces rapidly combine to produce a uniform pressure state within the molybdenum. During the period of peak pressure within the Mo sample, a quasimonochromatic x-ray source (XRS) (Cu He-α at 8.37 keV or 1.48 Å) was generated by focusing ∼8–12 Omega beams onto each side of a 2 mm × 2 mm copper foil (500 J beam^{-1} over 1 ns in a ∼250–400 μm spot). The ∼13-μm-thick Cu foil was positioned 24.3 mm from the target package and 45° from the target normal. Figure 3(a) shows a representative XRS laser pulse shape and time delay relative to the main sample drive. In most of our experiments, the x-ray drive consisted of a single laser pulse. However, in three shots, including the example shown in Fig. 3(a), the Cu foil was driven with two time-separated laser pulses (a pre-pulse and a main pulse) rather than with a single pulse. The configuration was aimed at achieving higher x-ray signal intensity. The pre-pulse had fewer beams (four beams with 500 J beam^{-1}) than the main pulse (12 beams with 500 J beam^{-1}) and preceded it by 3 ns.

X-rays scattered from the compressed Mo sample are collimated by the Ta pinhole and recorded as diffraction peaks on image plates (IPs) that line the walls of the diagnostic box [Fig. 2(c)]. To reduce the background noise level arising from the thermal emission from the drive plasma and to suppress the scattering intensity associated with the He-β line emission,

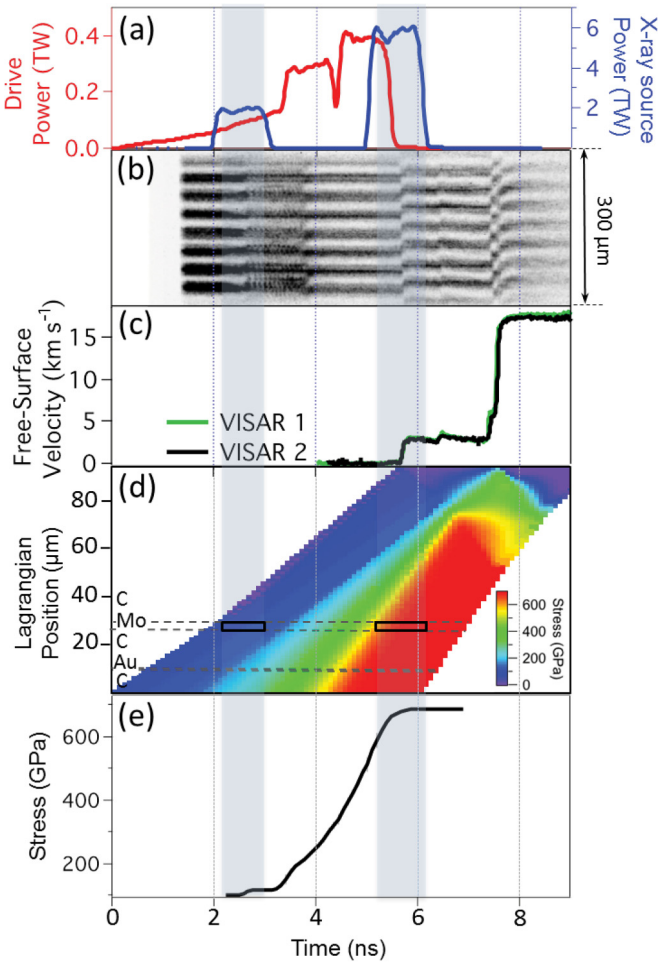

FIG. 3. (a) Representative laser pulse shapes for shot #68991 (628(40) GPa). The composite laser drive (red) consists of an initial ramp followed by a pair of 1-ns-long square pulses to increase and maintain the pressure. Intensity variations due to noise in the laser drive and timing misalignment of the pulses are smoothed during propagation through the ablator. The pulses used to generate the x-ray source (blue) for this shot consisted of an initial pre-pulse followed by a main pulse 3 ns later. The main pulse is timed relative to the loading pulse such that diffraction is recorded at the time of peak compression. (b) The VISAR record for this shot with fringe shifts recording the phase change associated with Doppler-shifted laser light reflected from the rear diamond surface. Rapid fringe modulation between 2.3 and 4 ns is due to a Fabry-Perot effect from interfering reflections from the moving Mo-diamond interface and the diamond free surface [66]. (c) Free-surface velocity history extracted from interferogram of (b) using two VISAR channels (black and green curves) with different velocity-per-fringe resolution. The first jump in velocity (to $\sim$3 km s^{-1}) is due to the elastic wave in the diamond and is followed by ramp loading to higher pressure. (d) Stress map in the target as a function of time calculated by back propagating from the free surface into the sample using the known equation of state of the diamond. Effects of wave interactions in the thin Mo sample and epoxy layers are ignored [53]. Positions of the diamond ablator, Mo sample, and diamond window are indicated by horizontal dashed lines. The x-ray probe times for the pre- and main pulses are shown by blue bands. (e) Calculated stress history at the center of the Mo sample.

25-μm-thick polyimide and $\sim$13-μm-thick Cu foils (spectral filters) are placed immediately in front of the IPs. Further details about the x-ray diffraction setup are provided elsewhere [49,53].

When the compression wave reaches the rear (diamond-vacuum) surface, it accelerates into free space. A 25-mm diameter opening in the back of the enclosure provides access for the VISAR [56] probe beam, which is used to measure the diamond window free-surface velocity history ($U_{\rm fs}$(t)). Figures 3(b) and 3(c) show the raw VISAR record and the extracted free-surface velocity history for a representative shot. The measured free-surface velocity profile and the previously measured EOS of diamond [45] are used to determine the stress state in the sample as a function of time through the method of characteristics in which the equations of motion are integrated backward in space and time to determine the stress history internal to the sample [53,54,58] [Figs. 3(d) and 3(e)]. The longitudinal stress is determined by averaging the values obtained in the sample region over the $\sim$ns probe period of the XRS pulse.

III. RESULTS

X-ray diffraction data from a representative experiment (shot #68991) are shown in Fig. 4. The data from five separate IPs are combined and projected into 2θ-ϕ coordinates [53], where 2θ is the diffraction angle and ϕ is the azimuthal

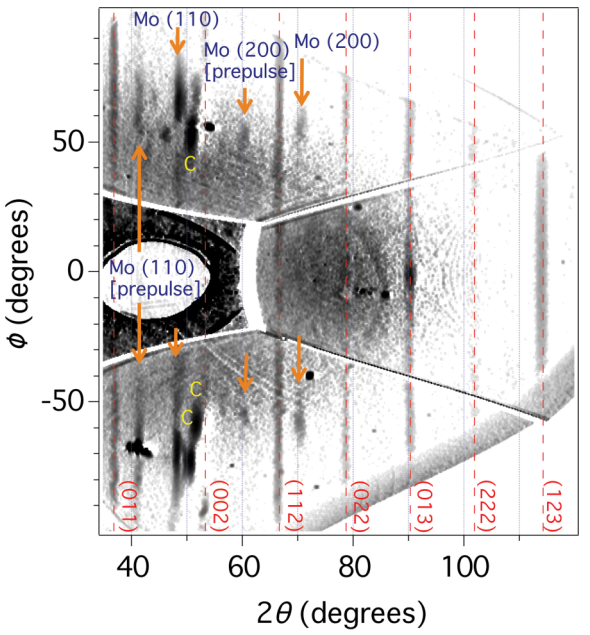

FIG. 4. Representative background-subtracted x-ray diffraction pattern of Mo (shot #68991) projected into 2θ-ϕ space [53], where ϕ is the azimuthal angle around the incident x-ray direction. The red vertical dashed lines show positions of ambient Ta x-ray diffraction peaks used for diffraction angle calibration. Orange arrows point to ramp-compressed Mo diffraction peaks arising from the x-ray pre-pulse (corresponding to 100(30) GPa) and at the later time of the main pulse (628(40) GPa). Diffraction peaks from the diamond windows are also indicated. The oval feature at the left is the VISAR aperture.

angle around the incident x-ray beam. In these coordinates, diffraction data project as straight lines of constant 2θ. All the observed diffraction lines in Fig. 4 can be assigned to one of the following: (1) the Ta pinhole (at ambient pressure), (2) compressed molybdenum, or (3) compressed diamond. The ambient-pressure Ta lines are used to calibrate the diffraction angle, 2θ (Fig. 4). Interplanar d spacings were determined from the diffraction angle using Bragg's Law: $\lambda = 2d\sin(\theta)$. The diffraction angle was determined to a typical precision of 0.1°, corresponding to a d-spacing uncertainty of $\sim$0.01 Å.

Diffraction lines observed at 2θ values of 48.4 and 70.1° can be assigned to the (110) and (200) reflections of bcc molybdenum compressed to 628(40) GPa, as determined by the characteristics analysis [Figs. 3(d) and 3(e)]. The (110) line is the most intense diffraction line of polycrystalline bcc Mo, and this corresponds to the strongest line observed in our experiments. We also observe the (200) or (211) Mo diffraction lines (expected intensities of 16% and 32% of (110)) in some shots. In experiments that used a pre-pulse in the x-ray drive, additional diffraction lines at higher d spacings were also observed. In the experiment shown in Fig. 4, these occurred at 2θ values of 41.6 and 60.5°. The d spacings for these two additional peaks correspond almost perfectly to the expected ratio of the d spacings of the two highest intensity peaks, (110) and (200), of a bcc structure, which have the relationship $d(110) = \sqrt{2}d(200)$. Characteristics plots for these experiments [Figs. 3(d) and 3(e)] show that the sample is at relatively low pressure at the time of the pre-pulse and reaches near peak pressures at the time of the main pulse. We interpret these additional lines as x-ray diffraction from the compressed Mo sample but at the lower pressures existing in the sample at the time of the pre-pulse [Figs. 3(d) and 3(e)].

Diffraction peaks arising from the diamond are also observed in our experiments. During the time window of the diffraction measurement while the sample is at peak compression, the diamond windows experience a large pressure gradient ranging from ambient up to the peak pressure [Fig. 3(d)]. The uniaxial compression modifies the initially single-crystal diamond peaks into increasingly distorted peak shapes, indicating that the diamond transforms to a highly textured polycrystal (as also observed in a previous ramp-compression x-ray diffraction studies [49,54]). Additional weak diffraction spots are also observed in some experiments and arise from Laue diffraction from single-crystal diamond generated by the x-ray background produced by the laser drive (Fig. 4).

Figure 5(a) shows diffraction patterns from one of the IPs at three selected pressures between 313 and 889 GPa. In all cases, a strong peak assigned to the highest intensity bcc Mo (110) peak is observed. This peak shifts to larger 2θ values (smaller d spacing) with compression, as expected. One-dimensional integrated diffraction patterns from selected areas on the IPs are shown in Fig. 5(b), with the corresponding peaks indicated. A strong (110) Mo peak is seen consistently in all experiments. Diffraction peaks that can be assigned to the Mo (200) and/or Mo (211) lines are also observed at lower pressures when not overlapped with Ta lines, but only the (110) line is observed at 889 GPa and above. This is the result of the decrease in signal-to-noise ratio due to higher background resulting from the stronger laser drive [53]. The maximum pressure reached was 1050(113) GPa.

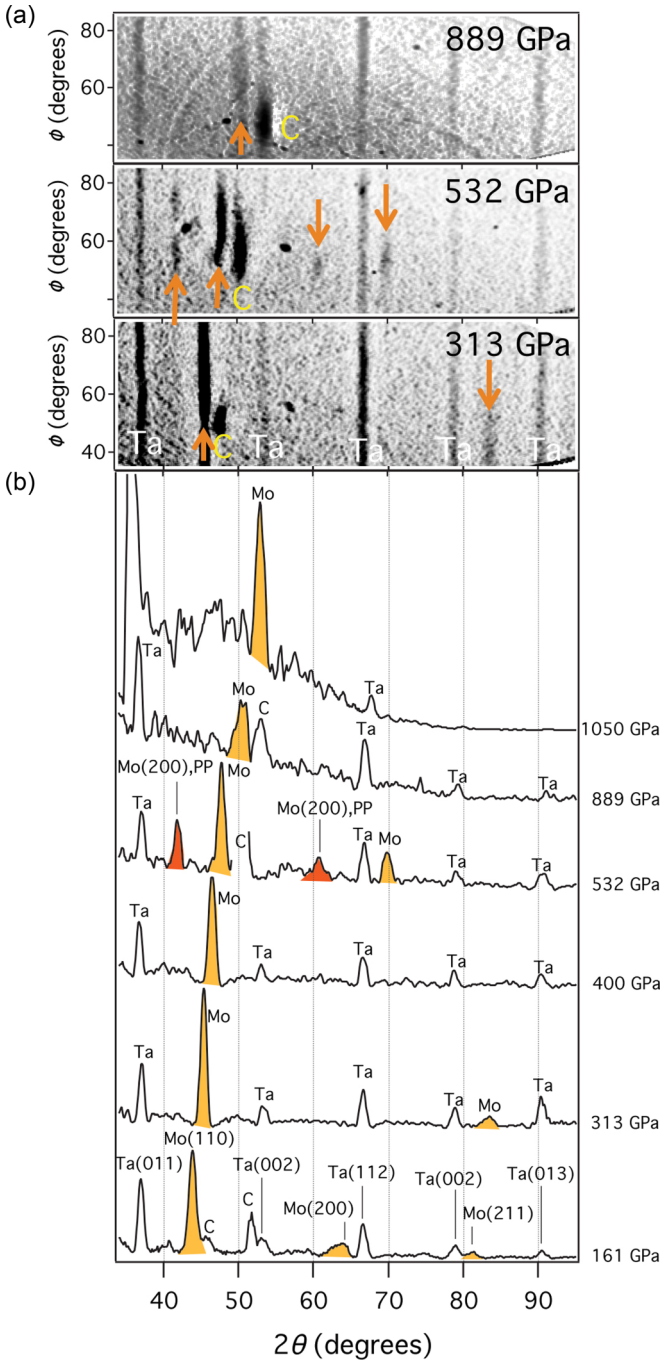

FIG. 5. (a) X-ray diffraction data from Mo at selected pressures from a representative image plate in 2θ-ϕ coordinates. Ambient-pressure tantalum diffraction peaks, Mo (orange arrows), and diamond diffraction lines are indicated. (b) Integrated one-dimensional x-ray diffraction patterns from selected experiments between 161 and 1050 GPa. Mo diffraction lines are shaded orange (main x-ray source pulse) and red (pre-pulse). Also shown are diffraction peaks from Ta and the diamond. Background subtraction has been performed.

The observed d spacings as a function of stress for our ramp-compressed Mo experiments are summarized in Fig. 6(a). The measured d spacings are compared with predicted 300-K values for bcc Mo (solid black line) calculated using the Vinet EOS [59] and previously measured values of the bulk modulus

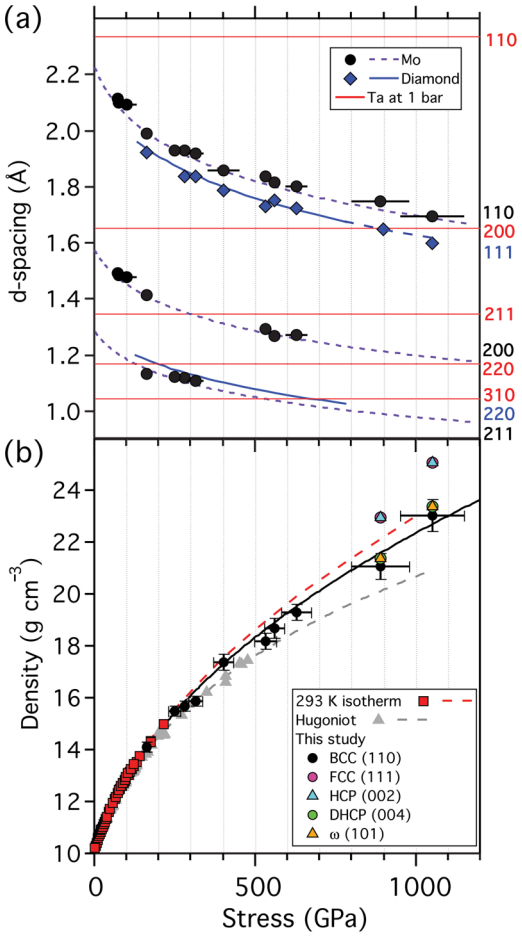

FIG. 6. (a) d spacing vs pressure for ramp-compressed Mo. The solid black circles show the (110), (200), and (211) d spacings of the bcc structure. The dashed purple curve shows the predicted positions of Mo peaks as a function of stress from extrapolation of static diamond anvil cell data [11,12]. The blue diamonds show the observed d spacings for peaks assigned to the diamond. The blue curve shows the calculated diamond d spacings from the EOS measured in a previous ramp-compression study [45]. Horizontal red lines show d spacings of Ta at ambient pressure. (b) Stress vs density for ramp-compressed Mo. The solid black circles show our ramp-compressed Mo data fitted to a Vinet EOS (black curve). Also plotted are static compression data [11,12] (red squares) and shock compression data [1,3,67–70] (gray triangles) and their extrapolations to higher pressures (red dashed [9] and gray dashed [10] curve, respectively). Calculated densities are also shown for possible assignment of the measured diffraction line above 900 GPa to the fcc, hcp, dhcp, and ω phases by assigning the measured Mo diffraction line to the indicated (hkl) reflection for each structure (see legend). For hexagonal phases (hcp, dhcp, and ω), the c/a ratios were taken to be 1.633, 3.154, and 0.622 [46,51–54], respectively. Uncertainties are shown for bcc only and are similar for other structures.

($K_0 = 261$ GPa) and its pressure derivative ($K_0' = \partial K_0/\partial P = 4.19$) [11,12]. The values of the d spacings assigned to Mo are consistent with those expected for a bcc structure, as can be observed within 4% agreement between our experimental data and the extrapolation of the bcc Mo EOS. In the three shots that used a pre-pulse in generating the XRS, the observed second pair of d spacings corresponding to the (110) and (200) Mo lines match well with the expected values at the stresses (100 GPa or less) calculated in the sample at the time of the pre-pulse [Figs. 3(d) and 3(e) and Fig. 6].

Over the entire measured compression range from 161 to 1050 GPa, we do not observe any discontinuity in d spacing or new diffraction lines that would be expected upon transition to another structure. Assuming the bcc structure, we determined the density of Mo up to 1 TPa from the experimentally measured d spacings [Fig. 6(b), see Table I]. Our ramp-compression data were fitted to the Vinet EOS assuming a fixed bulk modulus $K_0 = 261$ GPa [21], resulting in a pressure derivative of the bulk modulus along this compression path of $K_0' = 4.4(2)$. Observed peak positions assigned to the diamond are also shown in Fig. 6(a). The blue curve is obtained from previous ramp-compression measurements of the diamond up to 800 GPa [45], and they are in good agreement with the diffraction peaks from the diamond in this paper.

IV. DISCUSSION

Theoretical studies predict that Mo will transform from bcc to another close-packed structure (fcc or dhcp) above 600–700 GPa at 0 K [24,31,32,35–39]. We do not observe any evidence for a phase transition in the present paper. Below 600 GPa, we generally observe 2–3 diffraction lines at each pressure, and these are consistent with the bcc phase but not with other possible phases. At 889(100) GPa and above, we

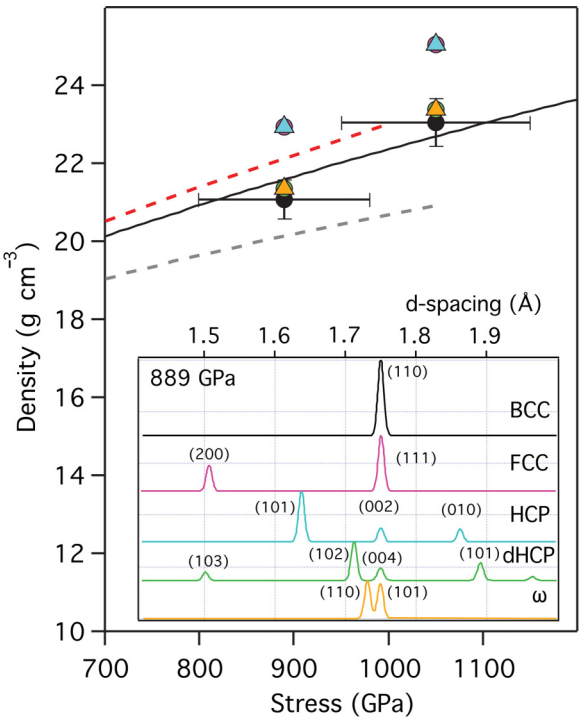

FIG. 7. Expanded view of stress-density data of Fig. 6(b) above 700 GPa. All symbols and lines are the same as in Fig. 6. The inset shows simulated powder diffraction patterns for possible Mo structures showing the diffraction peak for each structure that is the most plausible candidate to explain the observed line at 1.747 Å at 889(100) GPa. The corresponding density value for each assignment is shown in the main figure.

TABLE I. Results of x-ray diffraction experiments under ramp compression for solid Mo. d_{hkl} refers to d spacing of reflection hkl, and a is the unit cell parameter assuming a bcc structure.

Shot number	Stress (GPa)	d_{110} (Å)	d_{200} (Å)	d_{211} (Å)	a (Å)	X-ray Density (g cm^{-3})
68989[a,b]	70(5)	2.114(10)	1.494(9)		2.988(9)	11.9(2)
68987[a,b]	75(7)	2.10(11)	1.485(12)		2.970(12)	12.2(7)
68991[a,b]	100(8)	2.093(9)	1.481(10)		2.961(10)	12.3(4)
68985[b]	161(8)	1.999(8)	1.414(10)	1.152(10)	2.826(9)	14.1(2)
71108	250(24)	1.935(10)		1.118(12)	2.737(11)	15.5(2)
69811	279(14)	1.930(11)		1.116(10)	2.730(10)	15.7(2)
71105	313(28)	1.919(10)		1.109(10)	2.715(10)	15.9(2)
71111	400(36)	1.864(9)			2.636(9)	17.4(3)
68989[b]	532(33)	1.837(12)	1.295(13)		2.595(12)	18.2(3)
68987[b]	559(30)	1.819(12)	1.271(10)		2.572(11)	18.7(4)
68991[b]	628(46)	1.801(11)	1.274(11)		2.547(11)	19.3(3)
69815	889(100)	1.747(14)			2.471(14)	21.1(5)
72419	1050(113)	1.698(15)			2.401(15)	23.0(6)

[a]Indicates data from prepulse.
[b]Indicates shots using Mo foil; all others used polycrystalline pellets.

observe only a single diffraction line at $2\theta \sim 51^\circ$ [Fig. 5], and the observed d spacings at these pressures are consistent with the trend of the lower pressure data. In other words, we observe no evidence for a discontinuity in d spacing that might be expected in the case of a phase transition. Thus, our results suggest that Mo remains stable in the bcc structure under ramp compression to 1050 GPa.

To further explore whether a phase transition could be consistent with our data, we assigned the single diffraction line at our two highest pressures to major peaks from other possible structures and calculated the corresponding density. Figures 6 and 7 show the stress-density data and diffraction patterns for the bcc structure and other possible phases showing the most plausible (hkl) assignment for each to the peak observed experimentally at a d spacing of 1.747 Å. Assignment of this peak to hcp(101) or fcc(111) reflections would require a density increase of about 8% [Fig. 6(b)], assuming a c/a ratio of 1.633 for the hcp phase. We consider this unreasonable for two reasons. First, the density would be significantly higher than that expected along the 293-K isotherm, whereas ramp-loaded samples are expected to have densities intermediate between the room-temperature isotherm and the shock Hugoniot [Fig. 6(b)] [46]. Second, such a large volume change is unlikely for phase transitions at multimegabar pressures where phase changes typically involve only small volume changes [35,36].

We also checked the possibility of a phase transition to the omega (ω) phase. Omega is a hexagonal phase (space group $P6/mmm$) that has been identified as a possible candidate high-pressure phase for several transition metals [60], although theoretical density functional theory (DFT) calculations have suggested that it is not energetically competitive with other close-packed phases in Mo at high pressures [31]. Our observed line at 889(90) GPa could be explained by the ω phase ((101) peak) with a plausible density increase (∼2%) across the transition, assuming $c/a = 0.622$. However, the diffraction pattern of the ω phase consists of a closely spaced doublet of near equal intensities whose separation depends on the c/a ratio. The peak width (full width at half maximum) for the measured Mo line is 0.9–1.1° over the entire pressure range of our paper. If the peak separation of the ω phase doublet is less than about 1°, we would not be able to resolve it. We do not observe any evidence for peak broadening at the highest pressures, which would be expected in the case of an unresolved ω doublet. Hence, our data do not support a phase transition to the ω phase, although small ω distortions that produce a peak splitting below our resolution cannot be ruled out.

The dhcp structure may also match the observed diffraction line with a density of 21.9 g/cm^3 at 889 GPa if the observed line at 1.75 Å is assigned to the (004) peak of the dhcp structure [Fig. 6(b)]. This density is about 4% greater than that obtained for the bcc structure. The (004) diffraction line of the dhcp structure is expected to have relatively low intensity compared to other nearby dhcp peaks (31.8% and 68.9% of (102) and (101) lines, respectively). The (102) and (101) lines would be expected to occur at 2θ values of 52.6 and 47.5°, and no peak is observed at these angles. Strong preferential orientation in the sample could modify the relative peak intensities [61], but our data exhibit generally smooth intensity variation and there is no evidence for the extreme degrees of preferred orientation that would be required in this case (Fig. 4). Thus, the most plausible assignment of the observed diffraction peak is the persistence of the highest intensity (110) peak of the bcc structure.

For our two highest pressure experiments, the line assigned to the diamond (label C in Fig. 5) is consistent with d spacing trends from lower pressure data for this material as well as extrapolation of the results of Ref. [43]. However, we also checked the possibility that the lines assigned to the diamond at 889 GPa and 1050 GPa are instead due to diffraction from the Mo sample. We attempted to fit the resulting pair of possible sample lines to all the structures under consideration. The fcc and bcc structures could not match both lines. By varying the c/a ratio, we found that we could fit these two lines with the (004) and (102) peaks of the dhcp structure with a c/a ratio of 3.24–3.26. However, the resulting density is more than 7% larger than the bcc density (calculated from the (110) peak) at the same pressure or ∼6% smaller than extrapolated from our lower pressure bcc Mo data. Such a large density increase in a phase transition at these ultrahigh pressures is not likely, as discussed above.

The peak pressure achieved in our experiments was 1050(113) GPa, which is about 2.5 times higher than that achieved in static compression experiments on Mo. At the highest pressure, Mo attains a density of 23.0 g cm^{-3}, which corresponds to a factor of 2.3 compression for this incompressible metal. Our x-ray diffraction results are consistent with the persistence of the bcc phase of Mo to the highest pressures, and a phase transformation in Mo to fcc or dhcp (as predicted by DFT calculations [33,35,36,39] at 600–700 GPa and 0 K) is not observed (Fig. 1). A possible explanation is that the phase transition may need to be substantially overdriven in ramp compression experiments whose timescale may be fast relative to that required for formation of the high-pressure phase [62]. It is notable that in similar ramp compression experiments [49], the persistence of the bcc phase in tin has been observed up to 1200 GPa, well above the pressure for transition to the hcp phase (∼150 GPa at 0–300 K) from theoretical calculations and static experiments.

While the transition to a high-pressure phase from bcc Mo is predicted to occur at 600–700 GPa at 0 K, the effects of temperature on the transition are not well defined. The bcc phase is predicted on the basis of *ab initio* lattice dynamics calculations to be dynamically stable above 3500 K at 900 GPa and ∼6000 K at 1050 GPa [37], which suggests our experimental temperatures should lie above these values.

Temperature cannot be directly measured in our experiments [53,54]. A lower bound is given by the secondary isentrope (SESAME EOS table 2984) [63] (Fig. 1). The material response of diamond to ramp loading results in propagation of an initial elastic shock (to ∼80 GPa) followed by ramp compression to higher pressures after the diamond yields. This wave structure is then transmitted into our sample, which also experiences an initial shock followed by ramp loading. The secondary isentrope represents the isentropic compression path starting from the pressure-temperature (P-T) state set by the initial shock wave (Fig. 1). This temperature is likely to be a lower bound as a consequence of dissipation and material strength. Heating due to plastic work has been observed in ramp-compressed iron [64], and, given that Mo is also a strong, incompressible transition metal, its temperature along a ramp-compression path is also expected to be higher than the secondary isentrope. An upper bound to the expected temperatures in our experiments can be estimated from the secondary Hugoniot, which is a calculated double-shock state in which the first shock corresponds to the diamond elastic limit, and the shock brings the sample to the final pressure. Figure 1 shows the range of temperatures between the secondary isentrope and the secondary Hugoniot for molybdenum.

Based on *ab initio* molecular dynamics, the high-pressure phase transition is predicted to have a positive Clapeyron slope, which shallows with increasing temperature [33] (Fig. 1). Thus, the continued stability of the bcc phase observed here up to 1050(113) GPa may be a result of the positive Clapeyron slope of the transition or of an upper limit in the stability of the fcc/dhcp phase at high temperatures. Further theoretical studies of the very high P-T phase diagram of Mo are necessary in order to better understand the differences between our experimental results and theoretical predictions.

V. CONCLUSIONS

X-ray diffraction measurements of dynamically ramp-compressed molybdenum have been carried out over a wide pressure range from 70(5) to 1050(113) GPa. At all pressures, we observe from one to three diffraction lines that can be assigned to the bcc structure of Mo. The measured densities are intermediate between those achieved under shock compression and those expected from extrapolation of room-temperature static compression data, which is consistent with expectations for ramp-compressed solids. We do not observe evidence for the theoretically predicted transition to fcc or dhcp phases above 600 GPa, and our results support the continued stability of molybdenum in the bcc structure to 1050 GPa under ramp compression. These findings are expected to stimulate further theoretical and experimental work to better understand the behavior of this important material at ultrahigh pressures.

ACKNOWLEDGMENTS

We thank the OMEGA staff at the Laboratory for Laser Energetics (LLE) for laser operation and technical support. We also thank the Lawrence Livermore National Laboratory (LLNL) target fabrication team for their assistance. The research was supported by the National Nuclear Security Administration (NNSA)/Department of Energy (DOE) through the National Laser Users' Facility Program under Contracts No. DE-NA0002154 and No. DE-NA0002720. This paper was performed under the auspices of the U.S. DOE by LLNL under Contract No. DE-AC52-07NA27344.

[1] S. P. Marsh, ed., *LASL Shock Hugoniot Data* (University of California Press, Berkeley, 1980).
[2] R. S. Hixson, D. A. Boness, J. W. Shaner, and J. A. Moriarty, Phys. Rev. Lett. **62**, 637 (1989).
[3] R. S. Hixson and J. N. Fritz, J. Appl. Phys. **71**, 1721 (1992).
[4] P. D. Asimow, D. Sun, and T. J. Ahrens, Phys. Earth Planet. Inter. **174**, 302 (2009).
[5] T. S. Duffy and T. J. Ahrens, J. Appl. Phys. **76**, 835 (1994).
[6] C. E. Ragan III, M. G. Silbert, and B. C. Diven, J. Appl. Phys. **48**, 2860 (1977).
[7] J. Wang, F. Coppari, R. F. Smith, J. H. Eggert, A. E. Lazicki, D. E. Fratanduono, J. R. Rygg, T. R. Boehly, G. W. Collins, and T. S. Duffy, Phys. Rev. B **92**, 174114 (2015).
[8] J. H. Nguyen, M. C. Akin, R. Chau, D. E. Fratanduono, W. P. Ambrose, O. V. Fat'yanov, P. D. Asimow, and N. C. Holmes, Phys. Rev. B **89**, 174109 (2014).
[9] H.-k. Mao, P. Bell, J. Shaner, and D. Steinberg, J. Appl. Phys. **49**, 3276 (1978).
[10] Y. Wang, D. Chen, and X. Zhang, Phys. Rev. Lett. **84**, 3220 (2000).

[11] A. Dewaele, M. Torrent, P. Loubeyre, and M. Mezouar, Phys. Rev. B **78**, 104102 (2008).

[12] S. M. Dorfman, V. B. Prakapenka, Y. Meng, and T. S. Duffy, J. Geophys. Res. **117**, B08210 (2012).

[13] Y. K. Vohra and A. L. Ruoff, Phys. Rev. B **42**, 8651 (1990).

[14] A. L. Ruoff, H. Xia, and Q. Xia, Rev. Sci. Instrum. **63**, 4342 (1992).

[15] Y. Akahama, N. Hirao, Y. Ohishi, and A. K. Singh, J. Appl. Phys. **116**, 223504 (2014).

[16] D. Errandonea, R. Boehler, and M. Ross, Phys. Rev. B **92**, 026101 (2015).

[17] D. Santamaría-Pérez, M. Ross, D. Errandonea, G. D. Mukherjee, M. Mezouar, and R. Boehler, J. Chem. Phys. **130**, 124509 (2009).

[18] W. Liu, Q. Liu, M. L. Whitaker, Y. Zhao, and B. Li, J. Appl. Phys. **106**, 043506 (2009).

[19] K. D. Litasov, P. I. Dorogokupets, E. Ohtani, Y. Fei, A. Shatskiy, I. S. Sharygin, P. N. Gavryushkin, S. V. Rashchenko, Y. V. Seryotkin, Y. Higo, K. Funakoshi, A. D. Chanyshev, and S. S. Lobanov, J. Appl. Phys. **113**, 093507 (2013).

[20] X. Huang, F. Li, Q. Zhou, Y. Meng, K. D. Litasov, X. Wang, B. Liu, and T. Cui, Sci. Rep. **6**, 19923 (2016).

[21] T. S. Duffy, G. Shen, J. Shu, H.-k. Mao, R. J. Hemley, and A. K. Singh, J. Appl. Phys. **86**, 6729 (1999).

[22] P. Söderlind, R. Ahuja, O. Eriksson, B. Johansson, and J. M. Wills, Phys. Rev. B **49**, 9365 (1994).

[23] J. A. Moriarty, Phys. Rev. B **49**, 12431 (1994).

[24] A. B. Belonoshko, S. I. Simak, A. E. Kochetov, B. Johansson, L. Burakovsky, and D. L. Preston, Phys. Rev. Lett. **92**, 195701 (2004).

[25] L. Koči, Y. Ma, A. Oganov, P. Souvatzis, and R. Ahuja, Phys. Rev. B **77**, 214101 (2008).

[26] C. Cazorla, D. Alfè, and M. J. Gillan, Phys. Rev. B **85**, 064113 (2012).

[27] T. Lukinov, S. I. Simak, and A. B. Belonoshko, Phys. Rev. B **92**, 060101 (2015).

[28] D. L. Farber, M. Krisch, D. Antonangeli, A. Beraud, J. Badro, F. Occelli, and D. Orlikowski, Phys. Rev. Lett. **96**, 115502 (2006).

[29] A. Karbasi, S. K. Saxena, and R. Hrubiak, Calphad **35**, 72 (2011).

[30] J. A. Moriarty, Phys. Rev. B **45**, 2004 (1992).

[31] N. E. Christensen, A. L. Ruoff, and C. O. Rodriguez, Phys. Rev. B **52**, 9121 (1995).

[32] J. C. Boettger, J. Phys.: Condens. Matter **11**, 3237 (1999).

[33] A. B. Belonoshko, L. Burakovsky, S. P. Chen, B. Johansson, A. S. Mikhaylushkin, D. L. Preston, S. I. Simak, and D. C. Swift, Phys. Rev. Lett. **100**, 135701 (2008).

[34] C. Cazorla, D. Alfè, and M. J. Gillan, Phys. Rev. Lett. **101**, 049601 (2008).

[35] A. S. Mikhaylushkin, S. I. Simak, L. Burakovsky, S. P. Chen, B. Johansson, D. L. Preston, D. C. Swift, and A. B. Belonoshko, Phys. Rev. Lett. **101**, 049602 (2008).

[36] B. Wang, G. B. Zhang, and Y. X. Wang, J. Alloys Compd. **556**, 116 (2013).

[37] Z.-Y. Zeng, C.-E. Hu, W. Zhang, Z.-W. Niu, and L.-C. Cai, J. Appl. Phys. **116**, 133518 (2014).

[38] C. Cazorla, S. Binnie, D. Alfè, and M. J. Gillan, High Press. Res. **28**, 449 (2008).

[39] Z.-Y. Zeng, C.-E. Hu, L.-C. Cai, X.-R. Chen, and F.-Q. Jing, J. Phys. Chem. B **114**, 298 (2010).

[40] L. Dubrovinsky, N. Dubrovinskaia, E. Bykova, M. Bykov, V. Prakapenka, C. Prescher, K. Glazyrin, H.-P. Liermann, M. Hanfland, M. Ekholm, Q. Feng, L. V. Pourovskii, M. I. Katsnelson, J. M. Wills, and I. A. Abrikosov, Nature **525**, 226 (2015).

[41] R. G. Kraus, J.-P. Davis, C. T. Seagle, D. E. Fratanduono, D. C. Swift, J. L. Brown, and J. H. Eggert, Phys. Rev. B **93**, 134105 (2016).

[42] R. F. Smith, J. H. Eggert, R. Jeanloz, T. S. Duffy, D. G. Braun, J. R. Patterson, R. E. Rudd, J. Biener, A. E. Lazicki, A. V. Hamza, J. Wang, T. Braun, L. X. Benedict, P. M. Celliers, and G. W. Collins, Nature **511**, 330 (2014).

[43] J. Edwards, K. T. Lorenz, B. A. Remington, S. Pollaine, J. Colvin, D. Braun, B. F. Lasinski, D. Reisman, J. M. McNaney, J. A. Greenough, R. Wallace, H. Louis, and D. Kalantar, Phys. Rev. Lett. **92**, 075002 (2004).

[44] R. F. Smith, J. H. Eggert, A. Jankowski, P. M. Celliers, M. Edwards, Y. Gupta, J. Asay, and G. Collins, Phys. Rev. Lett. **98**, 065701 (2007).

[45] D. K. Bradley, J. H. Eggert, R. F. Smith, S. T. Prisbrey, D. G. Hicks, D. G. Braun, J. Biener, A. V. Hamza, R. E. Rudd, and G. W. Collins, Phys. Rev. Lett. **102**, 075503 (2009).

[46] J. Wang, R. F. Smith, J. H. Eggert, D. G. Braun, T. R. Boehly, J. R. Patterson, P. M. Celliers, R. Jeanloz, G. W. Collins, and T. S. Duffy, J. Appl. Phys. **114**, 023513 (2013).

[47] N. Amadou, E. Brambrink, A. Benuzzi-Mounaix, G. Huser, F. Guyot, S. Mazevet, G. Morard, T. de Resseguier, T. Vinci, K. Myanishi, N. Ozaki, R. Kodama, T. Boehly, O. Henry, D. Raffestin, and M. Koenig, High Energy Density Phys. **9**, 243 (2013).

[48] N. Amadou, E. Brambrink, T. Vinci, A. Benuzzi-Mounaix, G. Huser, S. Brygoo, G. Morard, F. Guyot, T. de Resseguier, S. Mazevet, K. Miyanishi, N. Ozaki, R. Kodama, O. Henry, D. Raffestin, T. Boehly, and M. Koenig, Phys. Plasmas **22**, 022705 (2015).

[49] A. Lazicki, J. R. Rygg, F. Coppari, R. Smith, D. Fratanduono, R. G. Kraus, G. W. Collins, R. Briggs, D. G. Braun, D. C. Swift, and J. H. Eggert, Phys. Rev. Lett. **115**, 075502 (2015).

[50] J. S. Wark, R. R. Whitlock, A. A. Hauer, J. E. Swain, and P. J. Solone, Phys. Rev. B **40**, 5705 (1989).

[51] J. Hawreliak, H. E. Lorenzana, B. A. Remington, S. Lukezic, and J. S. Wark, Rev. Sci. Instrum. **78**, 083908 (2007).

[52] D. Milathianaki, J. Hawreliak, J. M. McNaney, B. S. El-Dasher, M. D. Saculla, D. C. Swift, H. E. Lorenzana, and T. Ditmire, Rev. Sci. Instrum. **80**, 093904 (2009).

[53] J. R. Rygg, J. H. Eggert, A. E. Lazicki, F. Coppari, J. A. Hawreliak, D. G. Hicks, R. F. Smith, C. M. Sorce, T. M. Uphaus, B. Yaakobi, and G. W. Collins, Rev. Sci. Instrum. **83**, 113904 (2012).

[54] F. Coppari, R. F. Smith, J. H. Eggert, J. Wang, J. R. Rygg, A. Lazicki, J. A. Hawreliak, G. W. Collins, and T. S. Duffy, Nat. Geosci. **6**, 926 (2013).

[55] T. R. Boehly, D. L. Brown, R. S. Craxton, R. L. Keck, J. P. Knauer, J. H. Kelly, T. J. Kessler, S. A. Kumpan, S. J. Loucks, S. A. Letzring, F. J. Marshall, R. L. McCrory, S. F. B. Morse, W. Seka, J. M. Soures, and C. P. Verdon, Opt. Commun. **133**, 495 (1997).

[56] P. M. Celliers, D. K. Bradley, G. W. Collins, D. G. Hicks, T. R. Boehly, and W. J. Armstrong, Rev. Sci. Instrum. **75**, 4916 (2004).

[57] D. E. Fratanduono, T. R. Boehly, P. M. Celliers, M. A. Barrios, J. H. Eggert, R. F. Smith, D. G. Hicks, G. W. Collins, and D. D. Meyerhofer, J. Appl. Phys. **110**, 073110 (2011).
[58] S. D. Rothman, J.-P. Davis, J. Maw, C. M. Robinson, K. Parker, and J. Palmer, J. Phys. Appl. Phys. **38**, 733 (2005).
[59] P. Vinet, J. H. Rose, J. Ferrante, and J. R. Smith, J. Phys.: Condens. Matter **1**, 1941 (1989).
[60] J. E. Garcés, G. B. Grad, A. Fernández Guillermet, and S. J. Sferco, J. Alloys Compd. **289**, 1 (1999).
[61] H.-R. Wenk, S. Matthies, R. J. Hemley, H.-K. Mao, and J. Shu, Nature **405**, 1044 (2000).
[62] R. F. Smith, J. H. Eggert, D. C. Swift, J. Wang, T. S. Duffy, D. G. Braun, R. E. Rudd, D. B. Reisman, J.-P. Davis, M. D. Knudson, and G. W. Collins, J. Appl. Phys. **114**, 223507 (2013).
[63] S. P. Lyon and J. D. Johnson, Los Alamos National Laboratory Report No. LA-UR-92-3407 (1992).
[64] Y. Ping, F. Coppari, D. G. Hicks, B. Yaakobi, D. E. Fratanduono, S. Hamel, J. H. Eggert, J. R. Rygg, R. F. Smith, D. C. Swift, D. G. Braun, T. R. Boehly, and G. W. Collins, Phys. Rev. Lett. **111**, 065501 (2013).
[65] C. Dai, H. Tan, and H. Geng, J. Appl. Phys. **92**, 5019 (2002).
[66] D. E. Fratanduono, J. H. Eggert, T. R. Boehly, M. A. Barrios, and G. W. Collins, High Energy Density Phys. **11**, 26 (2014).
[67] J. M. Walsh, M. H. Rice, R. G. McQueen, and F. L. Yarger, Phys. Rev. **108**, 196 (1957).
[68] R. G. McQueen, S. P. Marsh, J. W. Taylor, J. N. Fritz, and W. J. Carter, in *High-Velocity Impact Phenomena*, edited by R. Kinslow (Academic Press, New York, 1970), pp. 293-417.
[69] K. K. Krupnikov, A. A. Bakanova, M. I. Brazhnik, R. F. Trunin, Dokl. Akad. Nauk SSSR **148**, 1302 (1963) [Sov. Phys.-Dokl. **8**, 205 (1963)].
[70] R. G. McQueen and S. P. Marsh, J. Appl. Phys. **31**, 1253 (1960).